Size and voltage dependence of effective anisotropy in sub-100-nm perpendicular magnetic tunnel junctions

Stephan K. Piotrowski, Mukund Bapna, Samuel D. Oberdick, Sara A. Majetich, Mingen Li, C. L. Chien, Rizvi Ahmed, and R. H. Victora

Phys. Rev. B **94**, 014404 — Published 5 July 2016

DOI: 10.1103/PhysRevB.94.014404

Size and voltage dependence of effective anisotropy in sub-100 nm perpendicular magnetic tunnel junctions

Stephan K. Piotrowski, Mukund Bapna, Samuel D. Oberdick, and Sara A. Majetich*

Department of Physics, Carnegie Mellon University

Mingen Li and C. L. Chien

Department of Physics & Astronomy, Johns Hopkins University

Rizvi Ahmed and R. H. Victora

Department of Electrical and Computer Engineering, University of Minnesota

(Dated: June 21, 2016)

Abstract

Magnetic tunnel junctions with perpendicular magnetic anisotropy are investigated using a conductive atomic force microscope. The 1.23 nm $Co_{40}Fe_{40}B_{20}$ recording layer coercivity exhibits a size dependence which suggests single domain behavior for diameters $\leq$ 100 nm. Focusing on devices with diameters smaller than 100 nm, we determine the effect of voltage and size on the effective device anisotropy K_{eff} using two different techniques. K_{eff} is extracted both from distributions of the switching fields of the recording and reference layers, and from measurement of thermal fluctuations of the recording layer magnetization when a field close to the switching field is applied. The results from both sets of measurements reveal that K_{eff} increases monotonically with decreasing junction diameter, consistent with the size dependence of the demagnetization energy density. We demonstrate that K_{eff} can be controlled with a voltage down to the smallest size measured, 64 nm.

PACS numbers: 85.75.-d,73.40.Gk,75.78.-n,75.70.-i

I. INTRODUCTION

Magnetic tunnel junctions (MTJs) with perpendicular magnetic anisotropy (PMA) are an attractive building block for non-volatile memories. PMA MTJs (p-MTJs) show promise in terms of the key requirements for implementation into products competitive with current data storage and memory technologies: large tunnel magnetoresistance (TMR), low writing energy cost, non-volatility over $\sim$ 10 years, and scalability of these properties toward $\sim$ 1 Tbit/inch^2 densities. Room temperature TMR ratios greater than 100% have long existed in in-plane MTJs[1,2]. In state of the art in-plane MTJs, TMR in excess of 600% is achieved by controlling the diffusion of Ta in the film stack through the addition of boron to the magnetic electrodes[3]. Despite these achievements, in-plane MTJs suffer from scalability issues due to their dependence on shape anisotropy for thermal stability and the high energy cost of switching the magnetization by the spin transfer torque (STT) effect[4,5]. For in-plane MTJs, switching energies $E_{\rm sw} = I_c^2 Rt$, where I_c is the critical switching current, R is the resistance, and t is the length of the pulse, of approximately 10 μJ/bit were achieved for current pulses on the order of 10 ms[6]. This value was drastically reduced using nanosecond pulses, yielding $E_{\rm sw}$ on the order of single pJ/bit in purely in-plane MTJs[7]. In high TMR p-MTJs the large out-of-plane demagnetization energy does not contribute to $E_{\rm sw}$[8]. Recently, TMR ratios up to 162% were obtained in p-MTJs by further controlling interlayer diffusion through the substitution of Ta with Mo in the film stack[9]. PMA is achieved when the CoFeB thickness is less than about 1.5 nm, so that the effective anisotropy $K_{\rm eff}$ is dominated by the interfacial anisotropy between Fe in the CoFeB and oxygen in the MgO[10]. In such p-MTJs, switching energies of hundreds of fJ/bit were achieved in 60 nm $\times$ 170 nm ellipses[11]. One of the most promising aspects of p-MTJs is that the interface anisotropy can be controlled by applying a bias across the tunnel junction[12–15]. This voltage controlled magnetic anisotropy (VCMA) effect is independent of STT. It can be combined with a magnetic field to switch p-MTJs at current densities on the order of 10^2 A/cm^2[14], about 4 orders of magnitude smaller than what is needed for STT switching. As a result, the magnetization state of p-MTJs can be reversed with very low energies. Grèzes *et al.* achieved switching energies of approximately 6 fJ for junction diameters of about 50 nm by exciting precessional motion using a 600 Oe

in-plane field combined with voltage pulses[16]. This is comparable to the energy associated with writing CMOS bits[17].

The scaling behavior of p-MTJs below the single domain (SD) limit is of particular interest. The coercivity is largest at the SD limit and scales with volume rather than domain wall energy below this limit. Although a large range of sizes has been studied in the literature, very few studies address the critical size for SD reversal[18,19]. In this paper, we present a study of devices with K_{eff} between roughly $1-2\times10^5$ erg/cc in the SD regime. We present transport measurements made with a conductive atomic force microscope (C-AFM) on $Co_{40}Fe_{40}B_{20}$/MgO/$Co_{40}Fe_{40}B_{20}$ MTJs with interfacial PMA patterned with reactive ion etch (RIE) processes. This builds on our previous work, where we have used C-AFM to measure the magnetoresistance of isolated magnetite nanoparticles on an FePt film[20], in-plane MTJs[21], and MTJs with interfacial PMA[22,23]. We focus on the effective recording layer anisotropy K_{eff} and the VCMA effect as a function of size in the SD regime. In one set of measurements, we extract K_{eff} by studying the switching field distributions (SFDs) obtained from minor TMR hysteresis loops. In a complimentary set of experiments, we determine K_{eff} from the statistics of random magnetization reversal as a function of time under thermally unstable conditions imposed by applying a magnetic field. These measurements are repeated for different bias voltages to determine $K_{\text{eff}}(V)$.

II. METHODS

A. Sample Preparation

The MTJ film stack was grown on thermally oxidized Si with the structure Si$\|$$SiO_2$/Ta(7)/Ru(26)/Ta(7)/$Co_{40}Fe_{40}B_{20}$(0.82)/MgO(2.1)/$Co_{40}Fe_{40}B_{20}$(1.23)/Ta(10)/Ru(20) where the numbers in parentheses are thicknesses in nanometers. The thin film deposition was carried out as in Ref.[14]. The coupon which was patterned came from a sample where the MgO thickness was varied linearly across the wafer. The thickness of 2.1 nm was chosen to minimize STT effects while maintaining an appreciable TMR. To pattern the film stack, a 30 nm thick Al mask was sputtered on top of the Ru layer and an additional 20 nm SiN_x mask was

sputtered on top of the Al. The negative tone resist hydrogen silsesquioxane (HSQ) was then spun onto the stack and patterns were written by electron beam lithography. Circular features were written in arrays containing 9 rows with the diameter varied by row. The diameters ranged from 550 nm to 40 nm. The arrays were repeated over a region covering approximately 300 μm $\times$ 200 μm. These patterns were then transferred through the bilayer hard mask and the remainder of the film stack using five RIE steps. The additional Al mask layer was critical during the etching of the top Ta layer with CF_4, which undercuts SiN_x. In the final step, the CoFeB/MgO/CoFeB trilayer was etched using a combination of Ar and methanol (CH_3OH). This chemistry etches Ta very slowly due to the formation of TaC_x and TaO_x, which are nonvolatile and mechanically hard. This ensures that our RIE process stops at the Ta electrode beneath the functional trilayer. Details of the etch chemistries used can be found in the Supplemental Information of Ref.[23]. After the dry etching processes, a wet rinse with a tetramethylammonium hydroxide based developer was performed to remove residual Al mask material. At the end of the patterning process, the top Ru layer was used as the electrical contact for transport measurements.

B. Conductive Atomic Force Microscope Measurement

Transport measurements were made using a conductive atomic force microscope (C-AFM) operated in contact mode (RHK UHV-350 with R9 controller). All measurements were done in atmosphere at room temperature with voltage bias applied between the sample and the probe. Here, positive bias denotes electrons flowing from the AFM tip into the top of the sample. Patterned nanopillars were located in scanning mode and individual devices were measured by placing the conductive probe directly on top of the device. Once a device was located, the exact position of the probe was finely adjusted to minimize the total resistance, corresponding to minimizing the contact resistance. The current through the device was then measured as a function of either perpendicular magnetic field or time. Measured currents were generally between hundreds of nanoamperes to several microamperes. The perpendicular field was supplied by an electromagnet below the sample stage and a maximum field of $\pm$800 Oe could be applied at the sample. For current versus field measurements conducted

to determine the TMR hysteresis loops the typical sweep rate was 340 Oe/s. Our experiments consisted of three types of measurements: Minor TMR hysteresis loops where only the recording layer was switched, major TMR hysteresis loops where both the recording and reference layers were switched, and traces of the TMR versus time with an applied field and bias chosen to impose thermal instability. These experiments were all repeated at multiple bias voltages.

Minor TMR loops of the recording layer were obtained by sweeping the applied magnetic field while measuring the tunnel current through individual devices. In minor loops, there is a shift due to the magnetostatic field of the reference layer at the recording layer but the recording layer coercivity is readily obtained from the loop width[22]. In major loops, the switching fields of the reference layer can also be observed but it is in general not possible to obtain the true coercivity of the reference layer[22]. To determine the effect of device diameter and bias on device TMR, recording layer coercivity, and magnetostatic loop shift, we recorded multiple minor loops for 36 devices spanning the range of nominal sizes between 550 nm to 60 nm. For each device characterized, we recorded approximately 30 loops at no fewer than 4 bias values between ± 1 V. To experimentally characterize the SFD, we conducted a more exhaustive set of experiments where approximately 100 minor loops were measured for various devices at several applied biases. We also collected TMR major loops for one device at several biases to compare the recording and reference layer SFDs.

Time traces of the TMR signal at fixed values of applied magnetic field were collected to study thermally activated magnetization reversal in the recording layer. First, the switching fields of the recording layer of a device were determined by collecting a TMR minor loop. Then, we initialized the MTJ in the high TMR state, with the recording and reference layers antiparallel. The applied field was then set to a value close to the recording layer switching field, causing it to fluctuate between the high and low TMR states as a function of time. A series of such time traces was recorded at multiple applied fields spaced by about 2 Oe. A range of fields was chosen so that the MTJ was almost entirely in the high TMR state at one end of the range and almost entirely in the low TMR state at the other end of the range. A sufficient number of time traces was collected at each field so that at least about 100 transitions between each state were recorded. In cases where the fluctuations occurred

relatively rapidly, over 1000 transitions were recorded. We repeated the measurements for multiple sample biases to study the VCMA effects as well.

C. Micromagnetic Simulations

Simulation of the recording layer switching behavior through micromagnetic simulations solving the Landau-Lifshitz-Gilbert (LLG) equation was attempted. The exchange interaction field, the perpendicular anisotropy field owing to the interface anisotropy, the magnetostatic interaction field of the layer and the field representing thermal fluctuations have been included while solving the LLG equation[24]. All simulations have been performed for square samples keeping the area the same as the circular experimental samples. A moderate roughness of about 0.07 nm has been included in our simulations considering the importance of roughness reported in Ref.[24]. To estimate the coercivity H_C numerically, magnetization curves ($M-H$) have been generated by varying the applied field H from +200 Oe to −200 Oe, a range sufficient to observe the switching of the samples under consideration. To reduce the computational burden, a sweep rate of 20 Oe/ns has been implemented throughout the analysis. Furthermore, to reduce the statistical errors arising from the random nature of the thermal fluctuations, each $M - H$ curve has been averaged over 100 data sets.

III. RESULTS AND DISCUSSION

A. General Characterization

Fig. 1(a) shows the AFM topography of a representative array of patterned MTJ pillars. The lateral pillar dimensions appear significantly larger than what is measured by scanning electron microscopy (SEM), shown in Fig.1(c). This is due to the large radius of curvature of our AFM probes (approximately 100 nm[25]) which were coated with a thick layer of Pt to minimize contact resistance and allow for large currents before failure[20–22]. The target device diameters during electron beam lithography were 100 nm, 90 nm, 80 nm, 70 nm, 60 nm, 50 nm, and 40 nm for the seven respective rows shown in Figs. 1(a)–(c) from top to bottom.

We also fabricated MTJs with two larger target sizes of 550 nm and 230 nm. We refer to these as "nominal diameters" because high resolution SEM of the fully patterned arrays revealed that the diameter varied by up to 10 nm between devices with identical target diameters. In Fig. 1(a), the nominally 100 nm devices have a height of 21 ± 2 nm. The height decreases to 15 ± 1 nm for nominally 60 nm pillars due to enhanced tapering effects at larger aspect ratio. This has no impact on the functional CoFeB/MgO/CoFeB MTJ trilayer, which is at the bottom of the patterned structure. Fig. 1(b) shows the C-AFM current map of patterned MTJ nanopillars at +100 mV bias. The uniform color of each device in the current map suggests that the current spreads through the entire diameter of the MTJ before reaching the MgO tunnel barrier. The resistance is therefore dominated by the tunnel junction resistance area (RA) product rather than changes in local contact resistance. Fig. 1(d) shows a plot of the resistance versus area obtained by measuring many devices with nominal sizes between 100 nm and 50 nm. These measurements were carried out by assuming that each measured device had a diameter exactly equal to the nominal diameter and averaging the resistance values obtained at each size. The error bars in Fig. 1(d) represent the standard deviation of these averages. The only sizable error bar appears at 50 nm, indicating that larger size variations were most prevalent for smaller devices. The dashed fit gives $RA = 2.64\,\mathrm{k\Omega} \cdot \mu\mathrm{m}^2$ with an uncertainty of about 5%. The contact resistance was usually smaller than approximately 200 Ω. The device resistance was therefore always several orders of magnitude larger than the contact resistance, making it unnecessary to explicitly correct for the contact resistance[26]. The color difference between MTJs within a particular row reflects the size variations between MTJs with identical nominal diameters. We determine the effective electrical diameter from the RA product by $D_{\mathrm{eff}} = 2\sqrt{(RA)/\pi R}$ and use this in calculations that are sensitive to MTJ diameter. The wedged shapes of some of the MTJs in the top row of Fig. 1(b) are a scanning artifact which occurs along the fast scan direction of the AFM tip, where poor electrical contact is made when the probe encounters the leading edge of a pillar. The artifact occurs on the opposite edge of the device for the reverse scan direction. Transport measurements are not affected by this artifact. Although current consistent with tunneling through MgO was observed in 40 nm MTJs, the smallest devices to exhibit sharp magnetization reversal were 60 nm in diameter.

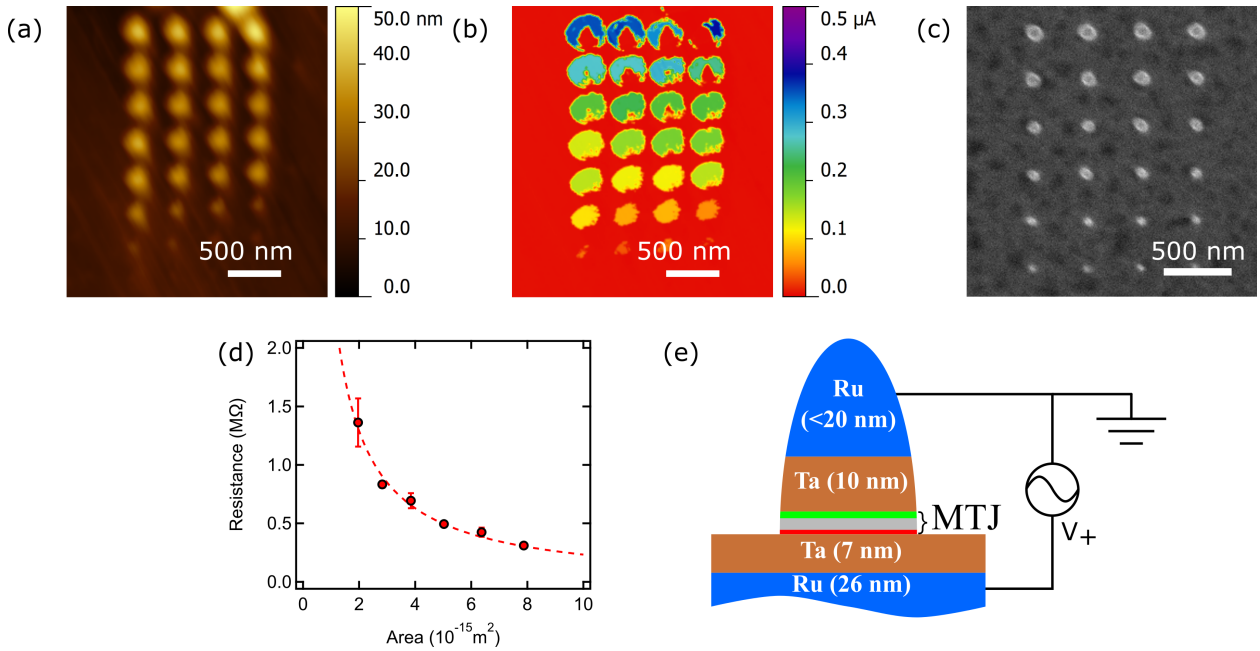

FIG. 1. (a) AFM topography and (b) C-AFM current map of patterned tunnel junctions at +100 mV bias. The fast scan direction is from the bottom to the top of the figures. (c) Scanning electron microscope image of a similar array on the sample. The rows correspond to the same nominal sizes as in the AFM topography. (d) Resistance versus area plot with dashed line showing constant $RA = 2.64\,\mathrm{k\Omega} \cdot \mu\mathrm{m}^2$. (e) Schematic of patterned film stack with the MTJ trilayer at the base of the etched structure. The recording layer (1.23 nm thickness) is shown in green while the reference layer (0.82 nm thickness) is shown in red. A schematic of the effective circuit is shown.

In Fig. 1(b), the sample-tip current is nearly zero when the tip is on the background rather than on top of a pillar. Along with the height information from Fig. 1(a), this suggests that the top exposed layer of the substrate is oxidized Ta and the top of the pillar is Ru. Although the Ru cap may also form a passive oxide, conduction in RuO_2 is metallic[27–29]. The fully patterned structure, with relative layer thicknesses to scale, is shown schematically in Fig. 1(e).

B. Size Dependence of Recording Layer Coercivity

In Fig. 2(a) we show characteristic TMR minor loops for three nominal sizes. Because the reference layer was magnetized up for these measurements, the minor loops have a negative magnetostatic shift. Fig. 2(b) shows the TMR as a function of effective diameter. We observed a slight reduction in TMR with decreasing diameter, consistent with other studies of methanol-etched perpendicular MTJs[30]. This is likely due to patterning effects such as disorder of the local crystal structure or stoichiometry at the edges. Such effects become more pronounced as the critical dimension is reduced and the edge region makes up a larger fraction of the total volume[30,31]. Fig. 2(c) shows the magnitude of the magnetostatic loop shift as a function of effective diameter. The loop shift increases steeply below 100 nm. Simulations show that the stray field from a thin magnetic disc is enhanced as the diameter is reduced[23,32]. The stray field is stronger near the edges of a magnetic disc and this effect becomes more pronounced as the disc becomes narrower. In Fig. 2(d) we show the recording layer coercivity as a function of D_{eff}. The coercivity drops sharply below 150 nm, which is consistent with the onset of single domain behavior. A similar size dependence is observed in Ref.[19], where the higher interface anisotropy alloy $Co_{20}Fe_{60}B_{20}$ was used along with a second MgO layer, resulting in a much higher K_{eff}. In SD particles, the coercivity is greatest at the largest SD diameter and decreases with decreasing size due to the influence of thermal energy[33]. For nucleation driven reversal modes, the demagnetization energy causes an increase in coercivity with decreasing size in a similar size regime[34]. Sato *et al.* have shown that the domain wall width is an excellent predictor of the diameter at which MTJs begin to exhibit single domain behavior[19]. The domain wall width is $\delta_w = \pi\sqrt{A_S/K_{\text{eff}}}$, where A_S is the exchange stiffness. Using 2×10^{-6} erg/cm as an approximate value for the exchange stiffness of CoFeB thin films[35] and $K_{\text{eff}} = 1.00 \times 10^5$ erg/cc (as shown in Section III E), we obtain $\delta_w \sim 140$ nm. We therefore argue that our devices with diameters of 100 nm and below are in the SD regime.

Micromagnetic simulation, as described in Section II C, showed an intermediate peak of the coercivity similar to the one in Fig. 2(d). However, the coercive field was much larger (150 Oe versus 80 Oe) owing to the reduced time scale (few ns per field increment) relative to the experiment. This allows thermal fluctuations less time to nucleate a domain and

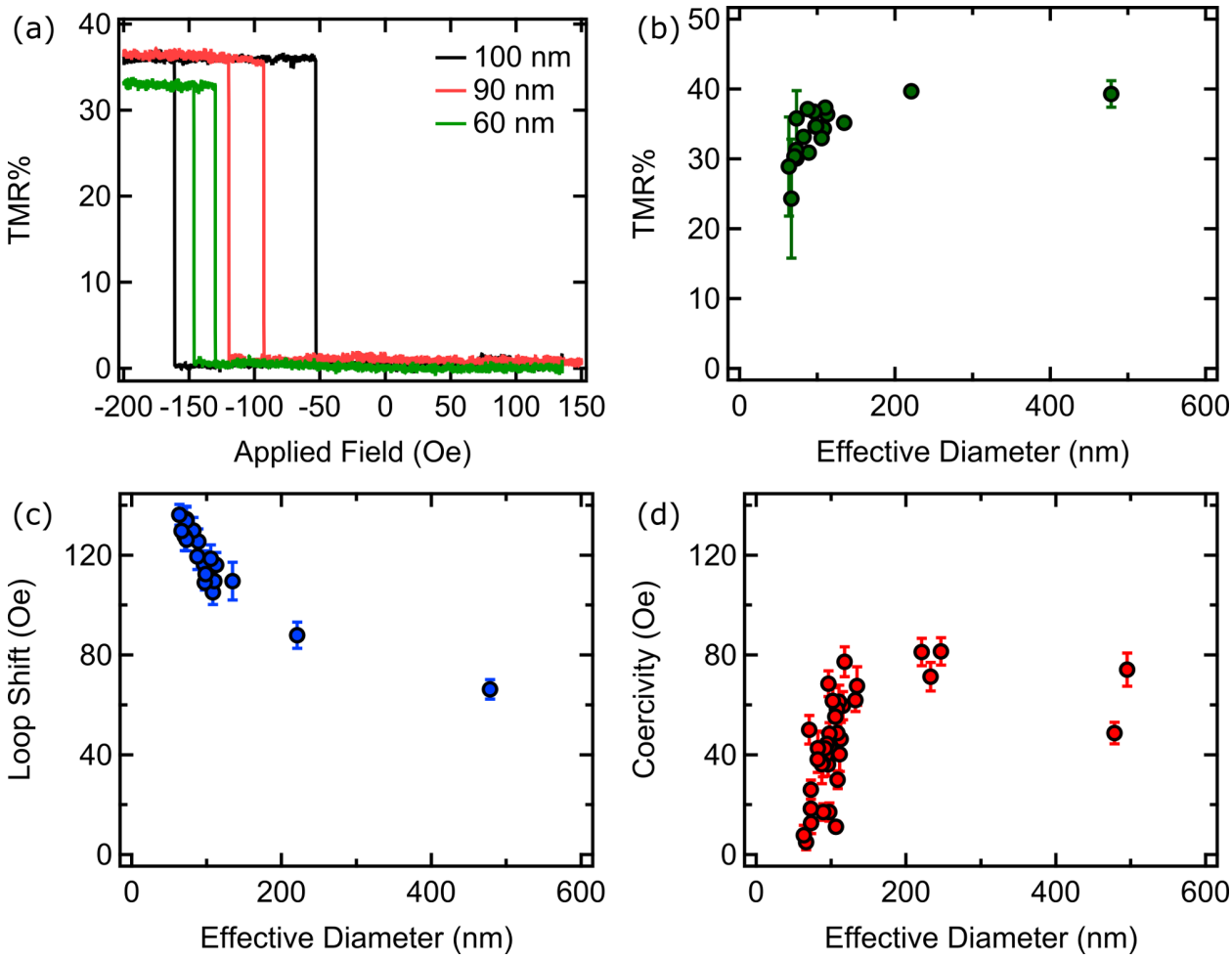

FIG. 2. (a) Characteristic TMR minor loops for three MTJ sizes, collected at −300 mV bias. (b) Device TMR, (c) magnitude of loop shift and (d) coercivity as a function of D_{eff}, measured at −300 mV. Individual data points correspond to results from single devices with error bars showing the standard deviation over repeat measurements of a particular device. Where error bars are not visible, they are smaller than the data points.

prematurely switch the sample. In fact, the micromagnetic loops were usually sheared, in contrast to the abrupt switching found experimentally. While reversal by coherent rotation was not usually observed, a geometrically incoherent process is consistent with a single domain remnant state[36].

For particles, the dependence of coercivity on diameter D has a complex but well-

understood form. The coercivity generally follows a power law $H_C \propto D^p$ where the value of p depends on the mechanism of magnetization reversal. The exponent can range from $p = 6$ for nanocrystalline materials with exchange coupled grains[37] to $p = 3$ for a single domain particle with uniaxial anisotropy and reversal by coherent rotation[38]. Fitting our data for $D_{\text{eff}} < 140\,\text{nm}$ to a D^3 power law gives reasonable agreement. The CoFeB in MTJs is known to be highly textured but polycrystalline[39–41]. We therefore expect that the magnetic layers in our MTJs have a polycrystalline structure with uniaxial anisotropy. In the multidomain regime, the coercivity is predicted to fall off as D^{-n} where n can vary between roughly $0.5 - 1$[42]. We do not have sufficient data for sizes larger than 200 nm to obtain a meaningful fit, but the reduction in H_C with increasing D is qualitatively consistent with multidomain behavior.

C. Switching Field Distributions

In Fig. 3(a), we show 10 TMR minor loops for the same nominally 80 nm MTJ at $-300\,\text{mV}$ where variations in switching fields from measurement to measurement can be qualitatively observed. For small volumes where thermal effects are important, the switching fields differ between measurements due to the stochastic nature of the reversal process. The left switch corresponds to the recording layer switching from antiparallel (AP) to parallel (P) relative to the reference layer and the right switch corresponds to the P to AP switch. In Fig. 3(b), we show the binned SFD of the AP to P (red) and P to AP (blue) switches obtained from 100 minor loops like the ones in Fig. 3(a). The switching fields do not have a normal distribution.

We predict an expression for the SFD σ by following the derivation by Garg[43] based on the escape rate over an energy barrier ΔE. The escape rate is the reciprocal of the characteristic dwell time between escape attempts given by an Arrhenious-Néel-Brown (ANB) law,

$$\tau = \tau_0 \exp(\Delta E / k_B T), \tag{1}$$

where k_B is the Boltzmann constant and T is the temperature. The multiplicative factor τ_0 is related to the attempt frequency f_0 associated with Larmor precession by $\tau_0 = f_0^{-1}$ and is approximately equal to 1 ns. The energy barrier can be derived by considering the

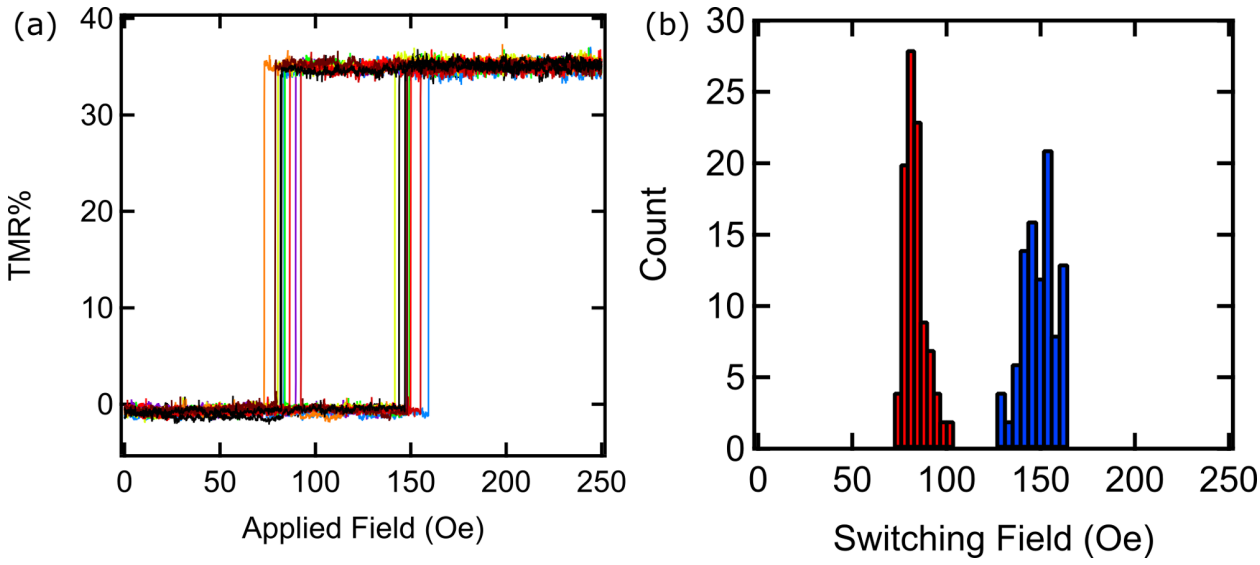

FIG. 3. (a) Ten TMR minor loops collected at −300 mV superimposed on each other for an 80 nm MTJ. (b) Binned switching field distribution of the switching fields from 100 minor loops.

total magnetic energy of a magnetic particle. For a particle with uniaxial anisotropy K and volume V in a net field $H_{\text{net}} = H - H_{MS}$ along the anisotropy (easy) axis the energy barrier is

$$\Delta E = E_0 \left(1 \pm \frac{H - H_{MS}}{H_a}\right)^2. \tag{2}$$

Here, $E_0 = KV$ is the anisotropy energy and $H_a = 2K/M$ is the switching field at zero temperature. The plus or minus sign depends on whether the field is parallel or antiparallel to the magnetization, with the plus sign taken in the former case. In the case of single domain reversal, K is the effective anisotropy $K_{\text{eff}} = K_b + K_i/t - E_d$ and V is the full volume of the magnet. Here, K_b is the bulk anisotropy, K_i is the interface anisotropy, t is the CoFeB thickness, and E_d is the demagnetzation energy density. In general, V may be some activation volume smaller than the full volume of the disc and K is then the local anisotropy of this subvolume. As noted earlier, Fig. 2(b) suggests the presence of process induced damage along the edges of the patterned devices. Others have modeled process induced damage in perpendicular Co/Pt multilayer pillars by assigning a reduced anisotropy to the outer few nanometers of the structures[44]. Kinoshita *et al.* concluded that for sufficiently small MTJs, process induced damage does not affect the reversal mechanism of perpendicular MTJs[30].

In this work, we assume some overall effective anisotropy that determines the energy barrier for magnetization reversal.

During a hysteresis loop measurement, the field is swept at a constant rate $R = dH/dt$. Equation (2) is therefore implicitly time dependent in this context, with $H(t) \propto R \cdot t$. The probability of not escaping over the energy barrier after time t is

$$P\left(H(t)\right) = \exp\left[-\int_0^t \left[\tau(t')dH/dt\right]^{-1} dt'\right]. \tag{3}$$

In perpendicular systems, this expression holds for current densities that are smaller than approximately half the critical STT current density[45]. Our measurements are done at current densities two orders of magnitude smaller than what is required for pure STT switching. In the ensuing discussion, we will explicitly correct for the magnetostatic field H_{MS} and so we set $H_{MS} = 0$. We obtain the appropriate Kurkijärvi-Fulton-Dunkelberger formula for the SFD from $\sigma = -d/dH[P(H)]$:

$$\begin{aligned}\sigma = & \\ &\left\{\frac{1}{\tau_0 R}\exp\left[-K_{\text{eff}}V(1 - HM_S/2K_{\text{eff}})^2/k_BT\right]\right\} \times \\ &\exp\left\{-\int_0^H \frac{1}{\tau_0 R}\exp\left[-K_{\text{eff}}V(1 - H'M_S/2K_{\text{eff}})^2/k_BT\right]\, dH'\right\}.\end{aligned} \tag{4}$$

The position of the maximum of this expression can be interpreted as the average coercive field. This position depends strongly on the value of K_{eff} because it appears as the argument of an exponential which is itself the argument of an exponential. The uncertainty in K_{eff} as a fitting parameter is therefore small when experimental SFDs have a well-defined peak.

1. Voltage Effects for Recording Layer

By obtaining the SFD for a particular device at multiple biases, we were able to isolate the effect of voltage on the anisotropy. Here, we will focus on the results for a single, nominally 80 nm diameter MTJ with $D_{\text{eff}} = 89$ nm, which will be referred to as Device A, for the discussion of the analysis. Fig. 4(a) shows characteristic TMR minor loops of Device A

at several biases. The reduction of TMR at larger magnitude biases is a well-documented phenomenon[46]. By recording 100 such loops at each bias, we obtained the coercivity as a function of bias, which is shown in Fig. 4(b). The error bars represent the standard deviation. The expected qualitative decrease of coercivity with more positive bias voltage caused by a reduction of the interface anisotropy[47] is evident. With our grounded C-AFM tip, positive bias leads to accumulation of negative charge in the recording layer near the MgO interface. In Fig. 4(c), we show the shift-corrected experimental SFD for the AP to P switch of the recording layer for Device A for several biases (solid markers). The shift correction was done by subtracting the average magnetostatic offset field at each bias from the raw switching fields at that bias. The switching fields at each bias were then binned and fit to Eq. (4) where the only fitting parameters were the effective anisotropy and an arbitrary normalization factor. The value $M_S = 1130\,\mathrm{emu/cc}$ was used[48] and the volume was calculated using D_{eff}. The nonlinear least-squares fits are shown as solid lines in Fig. 4(c). The general trend, observed for both the AP to P and P to AP switches in all three sizes, was for the SFD to broaden as the voltage (anisotropy) was reduced (increased). This is consistent with Eq. (4), which shows that the SFD broadens with increasing anisotropy at a fixed volume. In Fig. 4(d), we show the extracted fitting parameter K_{eff} as a function of bias for Device A (red dots) and two smaller devices (blue squares and green triangles). For positive bias values, the smaller devices did not produce clean hysteresis loops with deterministic reversal, but rather, exhibited multiple switches per field sweep direction. We attribute this to a sufficient reduction of K_{eff} by the voltage for thermal reversal events to occur faster than the time scale set by the field sweep rate. We therefore do not present an analysis of the SFD for these devices at positive biases. As such, although a clear bias dependence for K_{eff} can be seen for Device A, the data shown in Fig. 4(d) are too sparse to draw general conclusions about the effect of device size on the VCMA. An alternative approach will be shown below to quantify the VCMA effect as a function of size.

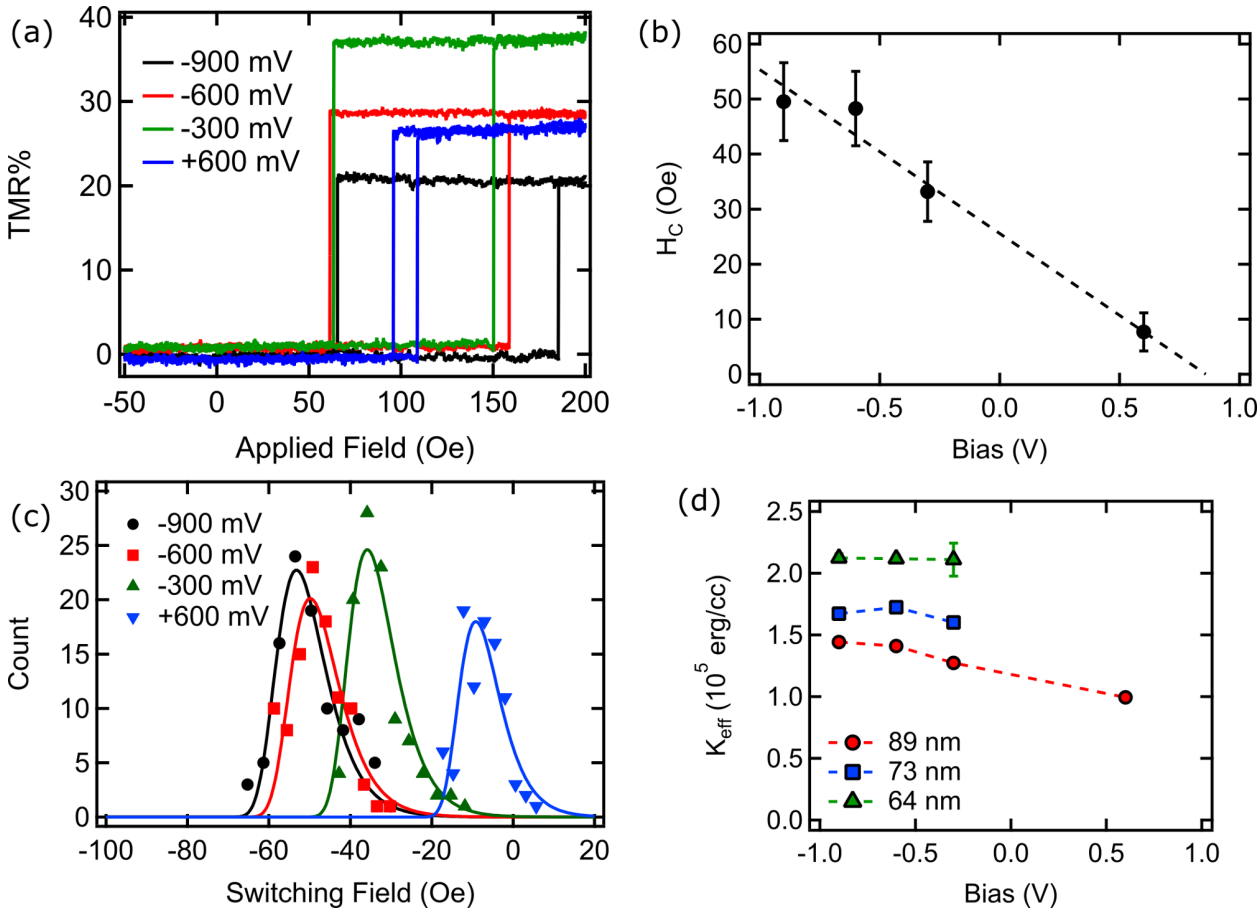

FIG. 4. (a) Characteristic TMR minor loops of Device A, a nominally 80 nm MTJ at 4 different applied biases. (b) Average coercivity of Device A as a function of bias for 100 measurements at each bias. Error bars represent the standard deviation for each set of measurements. (c) Shift corrected switching field distribution of the AP to P switch for Device A at each bias (filled markers) and fits to Eq. (4) (solid lines). (d) Bias dependence of K_{eff} for Device A (red circles) and two smaller devices (blue squares and green triangles). Error bars are smaller than the data points where they are not visible.

2. *Reference Layer Switching Field Distributions*

Fig. 5(a) shows a major loop for a $D_{\text{eff}} = 71\,\text{nm}$ MTJ at $-900\,\text{mV}$. The inner switches correspond to the recording layer and the outer switches to the reference layer. Unlike in a minor loop, where the reference layer is not reversed, the switching fields are nearly symmetric

about $H = 0$. As in the recording layer experiments, we collected 100 major loops for this device to obtain sufficient switching field statistics. Fig. 5(b) shows the experimental SFD for the reference and recording layers as filled circles. To fit the data to Eq. (4) without exact knowledge of the magnetostatic field, we let $H \rightarrow H - H_{MS}$. With the additional fitting parameter H_{MS}, the extracted values of K_{eff} had uncertainties ranging from about 30% to 60% whereas the values shown in Fig. 4(d) have uncertainties of approximately 1%. Nonetheless, K_{eff} for the reference layer was centered about values roughly twice as large as for the recording layer. The $2:3$ ratio of the reference layer thickness to the recording layer thickness is expected to result in the reference layer having a K_{eff} that is 1.5 times larger than the recording layer[8]. These results highlight the difficulty in characterizing the reference layer anisotropy by using the SFD analysis approach; when the magnetostatic field is not known, fits to Eq. (4) are far less rigorous.

D. Random Telegraph Noise and Anisotropy

The recording layer can be made thermally unstable by applying a field sufficiently close to its switching field if the anisotropy energy is sufficiently low. Alternatively, the temperature can be varied to destabilize a small magnetic particle. Hevroni *et al.* have recently investigated the temperature dependence of TMR fluctuations in magnetite nanoparticles on a Co film using scanning tunneling microscopy[49]. In our study, all experiments were done at room temperature. We will arrive at general findings by first presenting results from Device B, a 68 nm MTJ. Time traces of the TMR for Device B are shown in Fig. 6(a) at $H = 133\,\text{Oe}$ and in Fig. 6(b) at $H = 124\,\text{Oe}$. As the recording layer flips thermally, the MTJ TMR telegraphs sharply between zero and a maximum value corresponding to the reference and recording layers being parallel and antiparallel, respectively. The fraction of time spent in the two states clearly changes when the applied field is varied. The absence of any intermediate states reinforces our assertion of uniaxial anisotropy. We define τ_{P} to be the characteristic time spent in the P, low TMR, state and τ_{AP} to be the characteristic time spent in the AP, high TMR, state. The ANB model, Eq. (1), gives the characteristic dwell time in a magnetization state before reversal due to thermal fluctuations. As such,

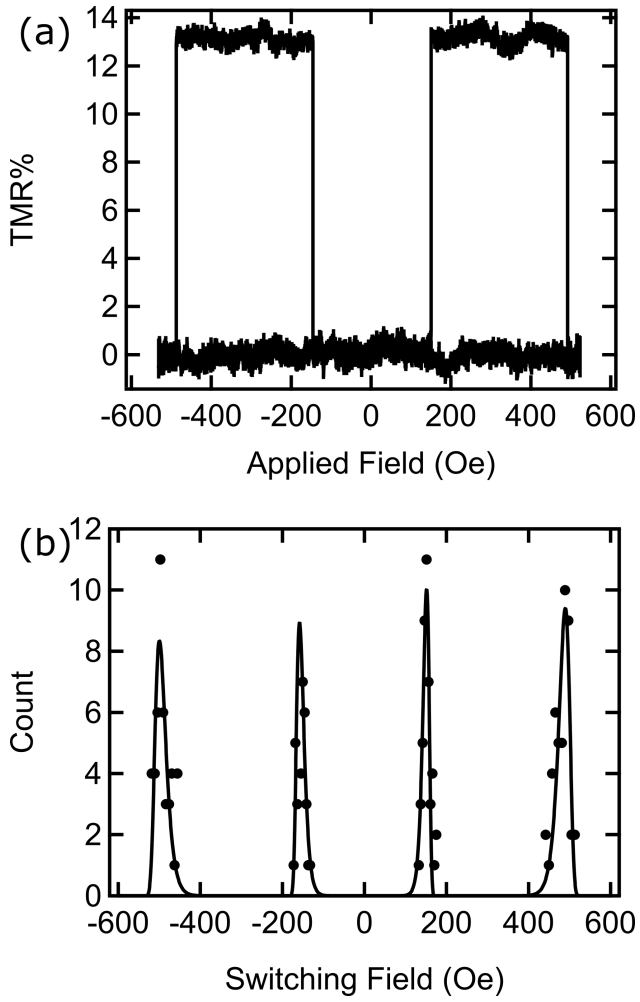

FIG. 5. (a) Characteristic TMR major loop of a 71 nm diameter MTJ at −900 mV bias. (b) Experimental SFDs for this device at −900 mV (filled circles) showing distributions for the recording layer (inner switches) and the reference layer (outer switches) with fits shown as solid lines.

the energy barrier ΔE can be probed rather directly by measuring the dwell times of the recording layer in the high and low TMR states while imposing thermal instability with an applied field. This approach places two practical restrictions on E_0 in Eq. (2), which sets an overall timescale for the thermal reversal process. First, E_0 must be small enough to obtain a sufficient number of switching events for a valid statistical analysis over a reasonable time frame. For our measurements, this corresponds to $\tau_{\mathrm{P(AP)}}$ being at most roughly several hundred milliseconds. Second, E_0 must be large enough that reversal events can be

well-resolved experimentally. Furthermore, the applied field must be restricted to values for which $\Delta E \approx E_0$ so that these conditions remain satisfied. In this context, measurements are only practical where the applied field is $H \approx H_{MS}$. It is therefore reasonable to expand Eq. (2) to first order around $H = H_{MS}$. This yields an approximate linear form of the energy barrier, $\Delta\tilde{E} = K_{\text{eff}}V \pm MV(H - H_{MS})$ for small variations in H around the loop center $H = H_{MS}$. By substituting this expression into Eq. (1), we obtain

$$e_T \ln(\tau/\tau_0) = K_{\text{eff}} \pm M(H - H_{MS}), \tag{5}$$

where $e_T = k_B T/V$.

To determine the values τ_{P} and τ_{AP}, we analyzed time traces of the TMR signal with a standard random telegraph signal approach. Each trace is composed of a collection of individual dwell times $\{\tau_{\text{P},1}, \ldots, \tau_{\text{P},m}\}$ and $\{\tau_{\text{AP},1}, \ldots, \tau_{\text{AP},n}\}$. The reversal process is described by Poisson statistics, and the "Poisson average" $\tau_{\text{P(AP)}}$ is obtained as the time constant in a fit of the distribution of the $\tau_{\text{P(AP)},i}$ to an exponential. Fig. 6(c) shows a plot of $e_T \ln(\tau_{\text{P(AP)}}/\tau_0)$ versus applied field for Device B. The natural logarithm of the dwell times clearly has a linear dependence on the applied field, in congruence with the approximate energy barrier $\Delta\tilde{E}$ and Eq. (5). A similar linear dependence has been reported for in-plane MTJs by others[50]. Fits of the data for τ_{P} and τ_{AP} to Eq. (5) are shown as dashed red and blue lines, respectively. The effective anisotropy is obtained where these fits intersect, i.e., where $\tau_{\text{P}} = \tau_{\text{AP}}$. The slopes of the τ_{P} and τ_{AP} fits are $-1400\,\text{emu/cc}$ and $2100\,\text{emu/cc}$, respectively. This is in accordance with our previous work, where we established an effect on the field dependence of the switching dynamics associated with the non-uniformity of the stray field from reference layer[23]. This effect reveals that corrections are necessary to the linear term in Eq. (5). The constant term, however, adequately determines the effective MTJ anisotropy. Fig. 6(d) shows a plot of K_{eff} as a function of sample bias for Device B (red circles) and two smaller devices (blue squares and green triangles) as obtained by this method. As with the SFD results discussed above, we observed that the anisotropy is voltage dependent and can be changed appreciably over a modest range of applied biases. For the SFD measurements, applying a broad range of voltages was not possible because smaller devices were not thermally stable enough to measure hysteresis loops at positive bias. The voltage dependence is

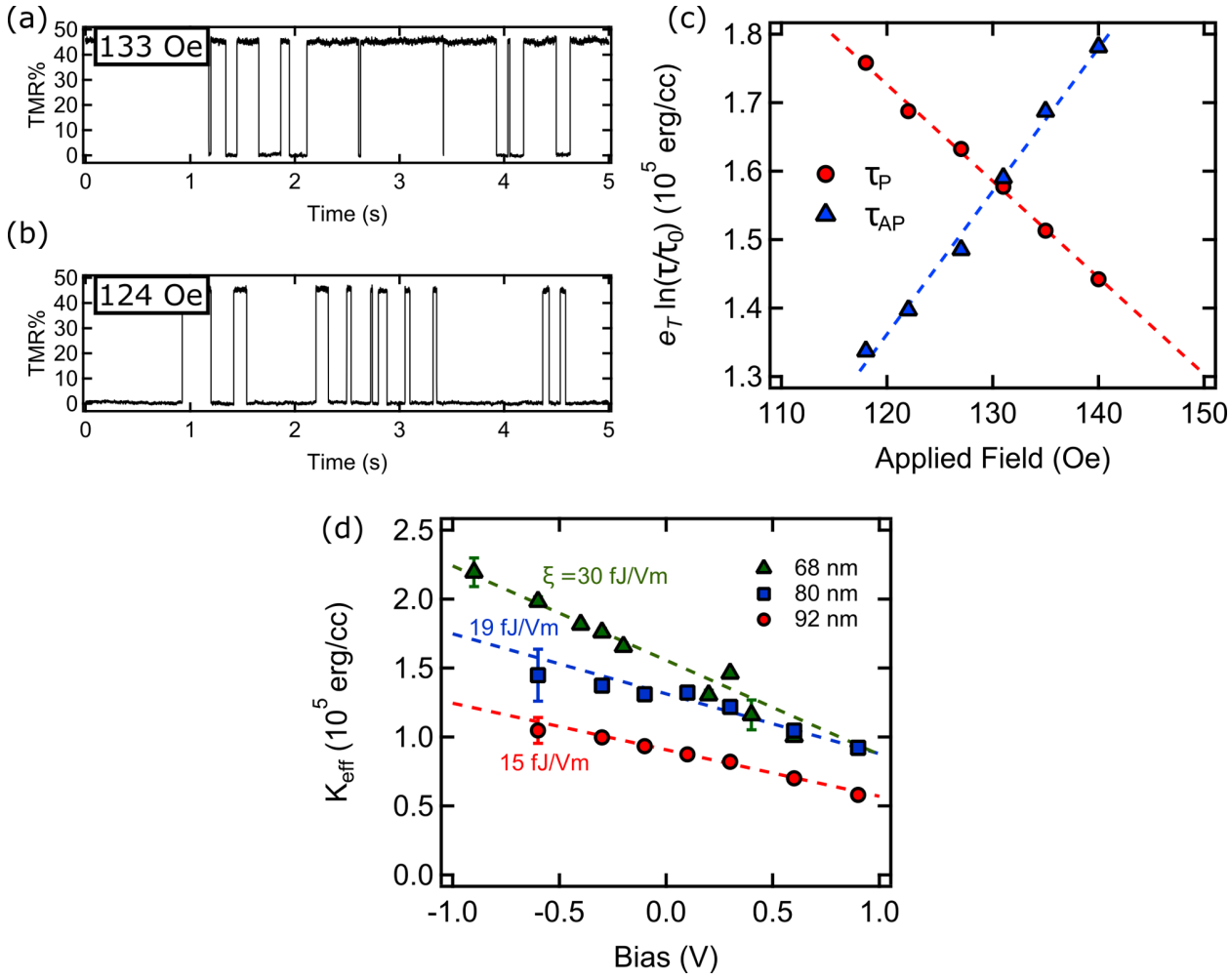

FIG. 6. TMR as a function of time for Device B, a 68 nm MTJ, at (a) 133 Oe and (b) 124 Oe. (c) Plot of $e_T \ln(\tau/\tau_0)$ versus applied field for Device B. Red circles show the low TMR dwell time τ_P and blue triangles show the high TMR dwell time τ_{AP}. Dashed lines are fits to Eq. (5). (d) Bias dependence of K_{eff} for three different devices obtained from analysis of the random telegraph signal. The VCMA efficiency ξ is shown beside linear fits (dashed lines) to each data set.

therefore unclear in Fig. 4(d). From the telegraph noise measurements discussed here, there is sufficient data to conclude that the effective anisotropy has the expected linear dependence on bias[14,51] down to $D_{eff} = 68$ nm. We determine the VCMA efficiency ξ, defined via

$$K_{eff} = K^0_{eff} - \xi \Delta V / t^2_{MgO}, \tag{6}$$

from linear fits to the data (dashed lines). Here, K^0_{eff} is the zero-bias device anisotropy,

ΔV is the bias across the MTJ and t_{MgO} is the MgO thickness. For these three devices with $D_{\mathrm{eff}} = 92\,\mathrm{nm}$, 80 nm, and 68 nm Eq. (6) gives $\xi = 15\,\mathrm{fJ/Vm}$, 19 fJ/Vm, and 30 fJ/Vm, respectively. The data for the $D_{\mathrm{eff}} = 89\,\mathrm{nm}$ device in Fig. 4(d) give $\xi = 14\,\mathrm{fJ/Vm}$, which is similar to the result for the nearly equally-sized 92 nm device shown here. The VCMA efficiencies we report here are similar to what others have reported[16]. Our results suggest that ξ may scale favorably as the junction diameter is reduced to sizes that are competitive with existing magnetic storage and CMOS technologies.

E. Size Dependence of Effective Anisotropy

Fig. 7 summarizes our measurements of K_{eff} as a function of size at an applied bias of $-300\,\mathrm{mV}$, combining the results of Sections III C and III D. The numerical values and their uncertainties are listed in Table I. K_{eff} varies by approximately a factor of 2 over the size range studied. This variation is consistent with the effect of the demagetization energy density, which becomes less negative as the diameter becomes smaller. The effective anisotropy is calculated by subtracting the demagnetization energy density $M_S^2(N_z - N_x)/2$ from the effective volume anisotropy, $K_v = K_b + K_i/t$. For a circular disc, $N_x + N_y + N_z = 2N_x + N_z = 4\pi$, and the resulting expression is

$$K_{\mathrm{eff}} = K_v - \frac{1}{2}M_S^2\left(\frac{3}{2}N_z - 2\pi\right). \tag{7}$$

The dashed line in Fig. 7 is a fit of the data to Eq. (7) from which we obtain $K_v = 7.98 \times 10^6\,\mathrm{erg/cc}$. Assuming that the bulk anisotropy is in-plane and that $|K_b| \approx 2\pi M_S^2$[28,52], the fit in Fig. 7 gives $K_i \approx 1.97\,\mathrm{erg/cm^2}$ for the recording layer. This result is in close agreement with other experimental results[53] as well as theoretical calculations[54] for MgO/CoFe/Ta structures.

IV. CONCLUSIONS

We have presented a study of the size and voltage dependence of the effective device anisotropy of SD p-MTJs using a conductive atomic force microscope. SFDs from hysteresis

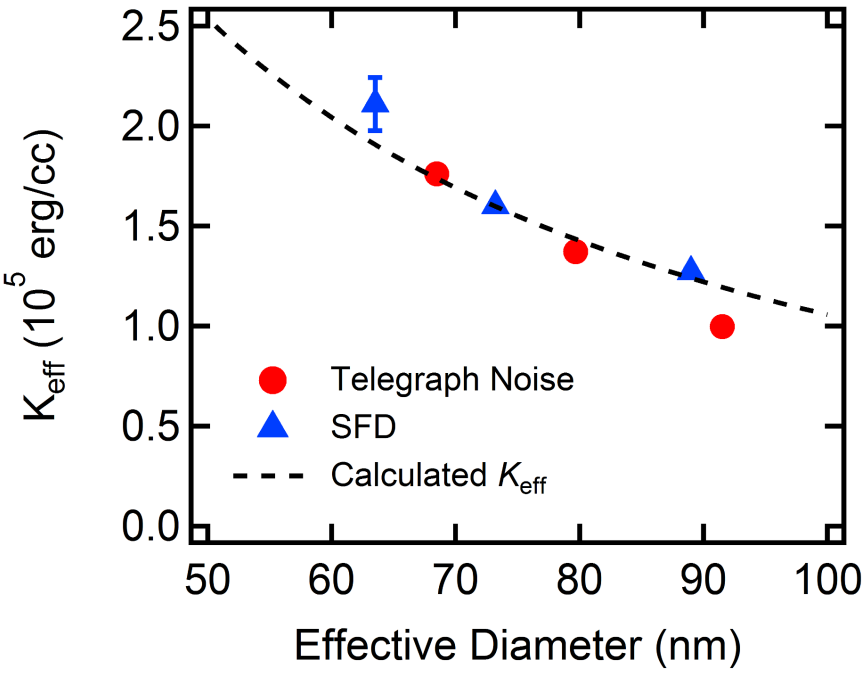

FIG. 7. Summary of K_{eff} at $-300\,\text{mV}$ obtained by random telegraph noise analysis (red circles) and analysis of the SFDs (blue triangles) for six devices of varying size. The dashed line shows a fit of K_{eff} given by Eq. (7) to the data.

loops recorded at several voltages were fit using an energy barrier model to obtain K_{eff}. For TMR minor loops this method determines K_{eff} of the recording layer to within an error of about 1%. However this approach is more difficult to apply to the reference layer SFDs in major loops due to the ambiguity of the exact value of the magnetostatic field of the recording layer. In that case the error in estimating K_{eff} is on the order of 30-60%. In a second set of experiments, we applied a magnetic field close to the switching field to induce thermal instability in the recording layer, and analyzed these data using a random telegraph signal approach. We determined K_{eff} by fitting the analyzed data to a linear approximation of the energy barrier to magnetization reversal. The recording layer switching fields at low bias voltage were consistent with SD behavior at and below diameters of 100 nm, in agreement with estimates of a domain wall width for the measured K_{eff}. Within the SD regime, results from both techniques revealed a size dependence consistent with demagnetization effects; K_{eff}

TABLE I. Values of effective MTJ anisotropy at $-300\,\mathrm{mV}$.

D_{eff} (nm)	K_{eff} (10^5 erg/cc)	Label
92	1.00 ± 0.02	
89	1.27 ± 0.01	*Device A*
80	1.37 ± 0.02	
73	1.60 ± 0.01	
68	1.76 ± 0.02	*Device B*
64	2.11 ± 0.13	

increased monotonically with decreasing junction diameter due to the suppression of the out-of-plan demagnetization factor. We show that with this approach, we can probe a broader range of anisotropies. We established a clear linear dependence of K_{eff} on the tunnel junction bias. The scaling that we report should translate to SD systems with higher anisotropies, where the SD regime begins at a smaller critical junction diameter. The VCMA effect persisted clearly in the smallest device studied using the random telegraph signal approach, 68 nm, with a VCMA coefficient of $\xi = 30\,\mathrm{fJ/Vm}$.

Our results provide insight into the scaling behavior of interfacial anisotropy systems below the single domain limit. In this regime, the energy required to reverse the magnetization depends on the volume of the device rather than the energy cost of nucleating a domain wall. For higher anisotropy structures, we expect similar size and bias dependences for K_{eff}. However, we expect large coercivities to persist at junction diameters well below 50 nm due to greater thermal stability.

ACKNOWLEDGMENT

This work was supported in part by STARnet, a Semiconductor Research Corporation program sponsored by MARCO and DARPA, under Contract 2013-MA-2831, by NSF Grant

ECCS-1407435, and by United States-Israel Binational Science Foundation Grant #2010137.

---

* sara@cmu.edu

[1] S. Yuasa, A. Fukushima, T. Nagahama, K. Ando, and Y. Suzuki, Japanese Journal of Applied Physics Part 2-Letters & Express Letters **43**, L588 (2004).

[2] S. Parkin, C. Kaiser, A. Panchula, P. Rice, B. Hughes, M. Samant, and S. Yang, Nature Materials **3**, 862 (2004).

[3] S. Ikeda, J. Hayakawa, Y. Ashizawa, Y. M. Lee, K. Miura, H. Hasegawa, M. Tsunoda, F. Matsukura, and H. Ohno, Applied Physics Letters **93**, 082508 (2008).

[4] L. Berger, Physical Review B **54**, 9353 (1996).

[5] J. Slonczewski, Journal of Magnetism and Magnetic Materials **159**, L1 (1996).

[6] Z. Diao, Z. Li, S. Wang, Y. Ding, A. Panchula, E. Chen, L.-C. Wang, and Y. Huai, J. Phys.: Condens. Matter **19**, 165209 (2007).

[7] G. E. Rowlands, T. Rahman, J. A. Katine, J. Langer, A. Lyle, H. Zhao, J. G. Alzate, A. A. Kovalev, Y. Tserkovnyak, Z. M. Zeng, and et al., Applied Physics Letters **98**, 102509 (2011).

[8] S. Ikeda, K. Miura, H. Yamamoto, K. Mizunuma, H. D. Gan, M. Endo, S. Kanai, J. Hayakawa, F. Matsukura, and H. Ohno, Nature Materials **9**, 721 (2010).

[9] H. Almasi, D. R. Hickey, T. Newhouse-Illige, M. Xu, M. R. Rosales, S. Nahar, J. T. Held, K. A. Mkhoyan, and W. G. Wang, Applied Physics Letters **106**, 182406 (2015).

[10] H. X. Yang, M. Chshiev, B. Dieny, J. H. Lee, A. Manchon, and K. H. Shin, Physical Review B **84**, 054401 (2011).

[11] P. Khalili Amiri, Z. M. Zeng, J. Langer, H. Zhao, G. Rowlands, Y.-J. Chen, I. N. Krivorotov, J.-P. Wang, H. W. Jiang, J. A. Katine, Y. Huai, K. Galatsis, and K. L. Wang, Applied Physics Letters **98**, 112507 (2011).

[12] R. Shimabukuro, K. Nakamura, T. Akiyama, and T. Ito, Physica E: Low-dimensional Systems and Nanostructures **42**, 1014 (2010).

[13] M. Endo, S. Kanai, S. Ikeda, F. Matsukura, and H. Ohno, Applied Physics Letters **96**, 212503 (2010).

[14] W. Wang, M. Li, S. Hageman, and C. Chien, Nature Materials **11**, 64 (2012).

[15] K. H. Khoo, G. Wu, M. H. Jhon, M. Tran, F. Ernult, K. Eason, H. J. Choi, and C. K. Gan, Physical Review B **87**, 174403 (2013).

[16] C. Grezes, F. Ebrahimi, J. G. Alzate, X. Cai, J. A. Katine, J. Langer, B. Ocker, P. Khalili Amiri, and K. L. Wang, Applied Physics Letters **108**, 012403 (2016).

[17] W. Wang, A. Pearse, M. Li, S. Hageman, A. Chen, F. Zhu, and C. Chien, Scientific Reports **3**, 1948 (2013).

[18] H. Sato, M. Yamanouchi, K. Miura, S. Ikeda, H. D. Gan, K. Mizunuma, R. Koizumi, F. Matsukura, and H. Ohno, Applied Physics Letters **99**, 042501 (2011).

[19] H. Sato, E. C. I. Enobio, M. Yamanouchi, S. Ikeda, S. Fukami, S. Kanai, F. Matsukura, and H. Ohno, Applied Physics Letters **105**, 062403 (2014).

[20] S. K. Piotrowski, M. F. Matty, and S. A. Majetich, IEEE Transactions on Magnetics **50**, 2303704 (2014).

[21] E. R. Evarts, L. Cao, D. S. Ricketts, N. D. Rizzo, J. A. Bain, and S. A. Majetich, Applied Physics Letters **95**, 132510 (2009).

[22] S. K. Piotrowski, M. Bapna, H. Almasi, W.-G. Wang, L. Tryputen, C. A. Ross, M. Li, C.-L. Chien, and S. A. Majetich, IEEE Transactions on Magnetics **51**, 4400504 (2015).

[23] M. Bapna, S. K. Piotrowski, S. D. Oberdick, M. Li, C.-L. Chien, and S. A. Majetich, Applied Physics Letters **108**, 022406 (2016).

[24] R. Ahmed and R. H. Victora, IEEE Transactions on Magnetics **51**, 4200104 (2015).

[25] E. R. Evarts, *Conductive Atomic Force Microscopy Analysis of Sub-30 nm Magnetic Tunnel Junction Nanopillars*, Ph.D. thesis, Carnegie Mellon University (2011).

[26] D. C. Worledge and P. L. Trouilloud, Applied Physics Letters **83**, 84 (2003).

[27] W. D. Ryden, A. W. Lawson, and C. C. Sartain, Physical Review B **1**, 1494 (1970).

[28] K. M. Glassford and J. R. Chelikowsky, Physical Review B **47**, 1732 (1993).

[29] K. M. Glassford and J. R. Chelikowsky, Physical Review B **49**, 7107 (1994).

[30] K. Kinoshita, H. Honjo, S. Fukami, H. Sato, K. Mizunuma, K. Tokutome, M. Murahata, S. Ikeda, S. Miura, N. Kasai, and et al., Japanese Journal of Applied Physics **53**, 103001 (2014).

[31] X. Peng, S. Wakeham, A. Morrone, S. Axdal, M. Feldbaum, J. Hwu, T. Boonstra, Y. Chen, and J. Ding, Vacuum **83**, 1007 (2009).

[32] J. Norpoth, S. Dreyer, and C. Jooss, J. Phys. D: Appl. Phys. **41**, 025001 (2007).

[33] F. E. Luborsky, Journal of Applied Physics **32**, S171 (1961).

[34] W. Stefanowicz, L. E. Nistor, S. Pizzini, W. Kuch, L. D. Buda-Prejbeanu, G. Gaudin, S. Auffret, B. Rodmacq, and J. Vogel, Applied Physics Letters **104**, 012404 (2014).

[35] H. Sato, M. Yamanouchi, K. Miura, S. Ikeda, R. Koizumi, F. Matsukura, and H. Ohno, IEEE Magnetics Letters **3**, 3000204 (2012).

[36] M. Sharrock, IEEE Transactions on Magnetics **35**, 4414 (1999).

[37] G. Herzer, IEEE Transactions on Magnetics **26**, 1397 (1990).

[38] D. J. Sellmyer and R. Skomski, *Advanced magnetic nanostructures*, 1st ed. (Springer, 2006) p. 376.

[39] K. Tsunekawa, D. D. Djayaprawira, M. Nagai, H. Maehara, S. Yamagata, N. Watanabe, S. Yuasa, Y. Suzuki, and K. Ando, Applied Physics Letters **87**, 072503 (2005).

[40] K. Tsunekawa, Y.-S. Choi, Y. Nagamine, D. D. Djayaprawira, T. Takeuchi, and Y. Kitamoto, Japanese Journal of Applied Physics **45**, L1152 (2006).

[41] Y. S. Choi, Y. Nagamine, K. Tsunekawa, H. Maehara, D. D. Djayaprawira, S. Yuasa, and K. Ando, Applied Physics Letters **90**, 012505 (2007).

[42] D. J. Dunlop, Physics of the Earth and Planetary Interiors **26**, 1 (1981).

[43] A. Garg, Physical Review B **51**, 15592 (1995).

[44] J. M. Shaw, S. E. Russek, T. Thomson, M. J. Donahue, B. D. Terris, O. Hellwig, E. Dobisz, and M. L. Schneider, Physical Review B **78**, 024414 (2008).

[45] D. B. Gopman, D. Bedau, S. Mangin, E. E. Fullerton, J. A. Katine, and A. D. Kent, Physical Review B **89**, 134427 (2014).

[46] X. H. Xiang, T. Zhu, J. Du, G. Landry, and J. Q. Xiao, Physical Review B **66**, 174407 (2002).

[47] C. Fowley, K. Rode, K. Oguz, H. Kurt, and J. M. D. Coey, J. Phys. D: Appl. Phys. **44**, 305001 (2011).

[48] W. G. Wang and C. L. Chien, J. Phys. D: Appl. Phys. **46**, 074004 (2013).

[49] A. Hevroni, B. Tsukerman, and G. Markovich, Physical Review B **92**, 224423 (2015).

[50] W. Rippard, R. Heindl, M. Pufall, S. Russek, and A. Kos, Physical Review B **84**, 064439 (2011).

[51] J. G. Alzate, P. K. Amiri, P. Upadhyaya, S. S. Cherepov, J. Zhu, M. Lewis, R. Dorrance, J. A. Katine, J. Langer, K. Galatsis, and et al., 2012 International Electron Devices Meeting , 29.5.1 (2012).

[52] D.-S. Lee, H.-T. Chang, C.-W. Cheng, and G. Chern, IEEE Transactions on Magnetics **50**, 3201904 (2014).

[53] T. Liu, J. W. Cai, and L. Sun, AIP Advances **2**, 032151 (2012).

[54] S. Peng, M. Wang, H. Yang, L. Zeng, J. Nan, J. Zhou, Y. Zhang, A. Hallal, M. Chshiev, K. L. Wang, and et al., Scientific Reports **5**, 18173 (2015).